Role of the carbon support on the oxygen reduction and evolution activities in $LaNiO_3$ composite electrodes in alkaline solution

Role of the Carbon Support on the Oxygen Reduction and Evolution Activities in LaNiO3 Composite Electrodes in Alkaline Solution

Caleb Alexander, Artem M. Abakumov, Robin Forslund, Keith P. Johnston, and Keith J. Stevenson

Just Accepted

Role of the Carbon Support on the Oxygen Reduction and Evolution Activities in LaNiO$_3$ Composite Electrodes in Alkaline Solution

Caleb T. Alexander[1], Artem M. Abakumov[2,3], Robin P. Forslund[4], Keith P. Johnston*[1], Keith J. Stevenson*[2]

[1]Department of Chemical Engineering, The University of Texas at Austin, Austin, Texas 78712, USA. [2]Center for Electrochemical Energy Storage, Skolkovo Institute of Science and Technology, 143026 Moscow, Russia. [3]Electron Microscopy for Material Science, University of Antwerp, Groenenborgerlaan 171, B-2020 Antwerp, Belgium. [4]Department of Chemistry, The University of Texas at Austin, 1 University Station, Austin, Texas 78712, USA. Correspondence and requests for materials should be addressed to K.J.S. (email: k.stevenson@skoltech.ru).

Keywords

Abstract

Metal-air batteries and fuel cells show a great deal of promise in advancing low-cost, high energy density charge storage solutions for sustainable energy applications. To improve the activities and stabilities of electrocatalysts for the critical oxygen reduction and evolution reactions (ORR and OER respectively), a greater understanding is needed of the catalyst/carbon interactions and carbon stability. Herein, we report how $LaNiO_3$ (LNO) supported on nitrogen-doped carbon nanotubes (N-CNT) made from a high yield synthesis lowers the overpotential for both the OER and ORR markedly to enable a low bifunctional window of 0.81 V at only a 51µg cm^{-2} mass loading. Furthermore, the addition of LNO to the N-CNTs improves the galvanostatic stability for the OER by almost two orders of magnitude. The nanoscale geometries of the perovskites and the CNTs enhance the number of metal-support and charge transfer interactions and thus the activity. We use rotating ring disk electrodes (RRDEs) combined with Tafel slope analysis and ICP-OES to quantitatively separate current contributions from the OER, carbon oxidation and even anodic iron leaching from carbon nanotubes.

Introduction

Sustainable sources of energy such as solar and wind, along with electric vehicles, need high energy density, low-cost energy storage to become economically viable[1]. For example, metal-air batteries show a great deal of promise as a route to increasing energy storage capabilities by reducing oxygen from air at the cathode to yield a theoretical energy density three to six times larger than conventional lithium insertion batteries[2]. The major bottlenecks for these devices, however, are the sluggish kinetics of the oxygen evolution reaction and oxygen reduction reaction (OER and ORR, respectively) which require a large overpotential to facilitate pragmatic current densities.[2,3] Additionally, the high cost of standard precious metal Pt and Ir OER and ORR catalysts is detrimental to wide-scale adoption.[4] A low-cost alternative to precious metals are perovskite oxides that have the formula $ABO_{3-\delta}$ where A is a lanthanide or alkaline earth element and B is a transition metal element[5,6]. Perovskite oxides have been shown to be catalytically active for both reactions,[7,8] have high oxygen diffusivity, [9,10] and may be synthesized using a wide variety of elemental compositions[7,11] for facile tuning of catalytic properties.

Several studies have shown that perovskites are highly active ORR catalysts, particularly when supported on N-doped carbons.[11–14] In alkaline conditions, the ORR proceeds by one of two major pathways, either the direct four electron route:

$$O_2 + H_2O + 4e^- \rightarrow 4OH^-\ E^o = +0.401\ V\ vs\ NHE \qquad (1)$$
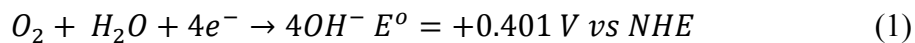
or by an initial two electron process where oxygen is first reduced to hydroperoxide:

$$O_2 + H_2O + 2e^- \rightarrow HO_2^- + OH^-\ E^o = -0.065\ V\ vs\ NHE \qquad (2)$$
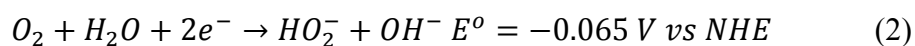
followed by electrochemical reduction to OH⁻ to complete what is commonly referred to as the 'two by two process':

$$HO_2^- + H_2O + 2e^- \rightarrow 3OH^- \quad E^o = +0.867\ V\ vs\ NHE. \qquad (3)$$
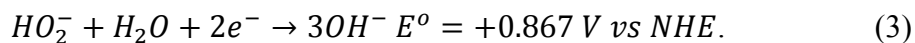
Furthermore, the hydroperoxide may be chemically disproportionated to O_2 and OH⁻ resulting in the 'pseudo-four electron process':

$$2HO_2^- \rightarrow O_2 +\ 2OH^- \qquad (4)$$

A more detailed description of the reaction 2 mechanism is briefly discussed in the SI. The direct four electron pathway typically occurs on materials such as Pt and its alloys while the hydroperoxide route typically occurs on most carbons and transition metal oxides.[15,16] In particular, N-doped carbon materials have been shown to be highly active for the ORR via the pseudo-four electron pathway.[13,17]

In contrast to the ORR, the OER has been shown to be more active on metal oxides and especially perovskites[7,18–20] relative to precious group metals. The adsorbate evolution mechanism (AEM) has been the most commonly accepted OER mechanism on perovskites since the work of Bockris and Otagawa,[8] but recently a new lattice oxygen mediated (LOM) mechanism has been demonstrated for certain perovskites containing oxygen vacancies.[19,21,22] The LOM mechanism occurs by utilizing lattice oxygen when the Fermi level dips into overlapping transition metal 3d and oxygen 2p bands that result in oxygen vacancies and a net lower activation energy barrier. Whereas these studies have been performed for perovskites mixed with supports including mesoporous N-doped carbon[11,19] and Vulcan carbon,[19] acetylene black[7] and Ketjenblack,[23] relatively few OER studies investigating perovskites have utilized carbon nanotubes which offer the benefit of highly accessible surface areas and higher electronic conductivities.[24–26]

Recent gains in characterizing the OER mechanism on perovskites provide a foundation for current attempts at understanding perovskite catalyst-support interactions.[27] One approach to promote charge transfer between the catalyst support and perovskite is to form covalent bonds

between transition metals and carbon, as reported for C-O-Mn bonds for $LaMnO_3$ perovskites to enhance the ORR.[28] However, a major challenge in forming perovskite-carbon hybrids with chemical bonds is the need for calcination at elevated temperatures to form the crystalline perovskite phase that often cannot be done in the presence of a support as it leads to preferential gasification of the carbon support. A promising alternative strategy to promote OER activity is to design the carbon support to be highly conductive, graphitic and have a morphology suitable to best electrically wire the perovskite catalysts to the electrode.

The stability of catalyst/carbon composites is a major challenge for the OER as the carbon support is thermodynamically unstable above ~0.09 V vs RHE and may be (electro)chemically oxidized to either CO or CO_2.[29,30] In an effort to solve this problem considerable efforts have been made to compensate for this thermodynamic instability by separating the OER and ORR half reactions[20], increasing the mass loading,[31] coating the carbon with TiO_2.[32,33] Efforts have also been made to slow the kinetic rate of carbon oxidation by designing perovskite composites with more stable, graphitic carbon supports.[25–27] The recently reported stability of various carbon-supported perovskites in rechargeable Zn-air batteries during cycling provides evidence that carbon may be used as a stable support under OER conditions[23,24]. In a study of the direct growth of N-CNTs on the surface of a $LaCoO_3$, the nanotube structure did not change after 37 h of galvanostatic polarization, but the degree of carbon oxidation was not quantified[25]. While these approaches have proven fruitful, it would be beneficial to measure directly the selectivity for the OER versus carbon oxidation to better understand the OER activity and how to improve catalyst stability.

Herein, we report a systematic study of the effect of carbon supports on the OER and ORR activity for a nanostructured electrocatalyst, $LaNiO_3$ (LNO). LNO was chosen because it is

highly active for the OER[18], can be reproducibly synthesized, and has been benchmarked versus other catalytically active, non-precious metal systems[11,18]. The high surface area and large aspect ratio of CNTs and N-CNTs in addition to the nanoscale geometries of the LNO are expected to raise the activities by enhancing the number of metal-support interactions and the overall electrical conductivity[27]. Additionally, N-CNTs are known to be highly effective supports for the ORR via the pseudo-four electron pathway in which the nitrogen functionality acts to increase the rate of the first two electron transfers[17,34]. The bifunctional window (the difference in potentials to reach 10 mA/cm$^2_{geo}$ for the OER and 3 mA/cm$^2_{geo}$ for the ORR [35]) for LaNiO$_3$ supported on N-CNTs was found to be only 0.81 V for the N-CNT/LNO composite at only 51 µg cm^{-2} loading, the lowest value reported to date for LaNiO$_3$. For the OER, we present a comprehensive methodology to delineate the effects of iron corrosion from the CNT supports, carbon corrosion, and oxygen evolution by combining RRDE measurements, Tafel slope analysis, and Fe concentration measurements with ICP-OES.

Experimental

Chemicals

All chemicals were used as received. Lanthanum (III) nitrate hexahydrate (99.995%), nickel (II) nitrate hexahydrate (99%) were purchased from ARCOS Organics. 5 wt % Nafion solution in lower alcohols, diethylene glycol (DEG, 99%), m-xylene (>99%) and ammonia gas (99.98%) were purchased from Sigma-Aldrich. Citric acid (100%), pyridine (99.9%), and ethanol (Absolute 200 proof) were purchased from Fischer Scientific and ferrocene (99%) was obtained from Alfa Aesar. Oxygen (research grade, 99.999% purity), argon (research grade, 99.999% purity) and hydrogen (research grade, 99.999% purity) were obtained from Praxair.

Millipore deionized water (18 MΩ cm) was used. Vulcan Carbon XC-72R (VC) was purchased from Cabot Corp.

N-CNT/CNT Synthesis

Nitrogen doped and non-doped carbon nanotubes were produced from a combination of prior floating catalyst CVD methods to increase total yield[34,36] using two single-zone tube furnaces (Carbolite Model HST 12/35/200/2416CG). 104.3 mg of ferrocene was placed in a small vial, capped with a rubber septum, and flushed with Ar to remove oxygen. 1 mL of pyridine was added to the vial to make a 9.6 wt% ferrocene solution. 1.0 mL of solution was loaded into a gas tight glass syringe (Hamilton 81320) and then interfaced with plastic tubing that led to the inlet of a sealed quartz tube (22 mm ID, 19.7 cm reaction zone length) as shown in Figure S1. The first zone and second zone were heated to $200^{o}C$ and $760^{o}C$, respectively, followed by a five-minute hold to reach equilibrium while Ar was purged at 200 sccm. The NH_3 and Ar flow rates were then raised to 56 sccm and 694 sccm for a total of 750 sccm using electronic gas mass flow controllers (MKS Type 1479A). The pyridine-ferrocene solution was then injected into the first stage furnace at 1.2 mL/hr using a programmable syringe pump (New Era Pump Systems NE-1000) for a total of 60 min after which both furnaces could cool to room temperature under Ar at 200 sccm. Previous approaches yielded only ~10 mg batches[34,37], but by modifying the synthesis conditions[36] N-CNTs were collected from the deposited film on the inside of the quartz tube with a typical yield of ~100 mg or 0.728 mg/cm^2, a ten-fold increase in product over prior studies[17,37]. Undoped CNTs were prepared as above except m-xylene was used instead of pyridine, NH_3 was not used, and Ar flowed at 750 sccm during synthesis which gave a total yield of ~350 mg or 2.55 mg/cm^2.

LaNiO₃ Synthesis

LNO was prepared via a modified Pechini method[38]. Briefly, 2.5 mmol of La and Ni

nitrates each were added to 50 mL of DI water containing 5 mmol of citric acid to produce a 1:1

metal ion to citric acid molar ratio. The solution was put onto a hot plate in a fume hood, stirred

and 3.33 mmol of DEG was added to the solution. A gel formed when all of the water had

evaporated. The gel then combusted with a visible flame and left behind metal oxide

constituents. The metal oxides were calcined in a furnace under dehumidified air (150 mL/min)

at 1^oC/min from 30^oC to 700^oC, held at 700^oC for 4 hours and then allowed to cool to room

temperature. The resulting LNO was washed three times with DI water and ethanol followed by

ball milling for three min.

Materials Characterization

X-Ray Diffraction (XRD) patterns were taken on a Rigaku Spider instrument with a Cu

Kα radiation (λ=1.5418 Å) source at 40 kW and 40 mA. Diffraction rings were integrated, and

JADE software was used to analyze peak patterns. Samples were analyzed with XPS using a

Kratos AXIS Ultra DLD (Al α radiation, λ=1.4866 eV) with high resolution spectra taken at 0.1

eV steps with 1 s, 1.5 s, 2.5 s, 2.5 s dwell time for C 1s, N 1s, O 1s, and Fe 2p regions,

respectively. Raman spectra were taken of the N-CNTs and CNTs using a Renishaw inVia

system with an Ar laser (λ=514.5nm, $3mW/cm^2$ and 50x aperture (NA=0.75) calibrated using a

silicon crystal standard. Sample diameter cross section is approximately 2 μm and spectra were

taken with a single 120 s long scan. Iron content was found using thermogravimetric analysis

(TGA) with a TA Instruments Q500 with 1-5 mg sample sizes in alumina crucibles. The

temperature was ramped from 25^oC to 900^oC at 20^oC/min under flowing air (Praxair 99.998%) at

50 mL/min to the sample. The N-CNT TEM specimen was prepared by crushing the sample in

an agate mortar under ethanol and depositing a few drops of suspension on a porous carbon grid

on a Cu support. High resolution transmission electron microscopy (TEM) images, high angle

annular dark field scanning TEM (HAADF-STEM) images, energy dispersive X-ray (EDX) and

electron energy loss (EELS) spectra were collected with an image and probe aberration-corrected

Titan G3 electron microscope equipped with EDAX detector and Quantum GIF spectrometer.

The microscope was operated at 300 kV. Surface areas of samples were measured with a

Quantachrome Instruments NOVA 2000 high-speed surface area BET analyzer at 77 K. Samples

were degassed for 4 hours at $120^{o}C$ prior to analysis and a P/P_o range of 0.05 to 0.30 was used to

determine the surface area. ICP-OES measurements were made in triplicate using a Varian 710

instrument with using argon gas and 2 wt% trace metal nitric acid as the sample carriers with a

1.2 kW plasma torch. Standards were made via serial dilution of a 10 mM $Fe(NO_3)_3$ solution in 2

wt% trace metal nitric acid.

Electrochemical Measurements

Electrochemical testing was performed on either a CH Instruments CHI832a or a

Metrohm Autolab PGSTAT302N with high speed rotators from Pine Instruments. All samples

were ball milled for three minutes and 30 wt% LNO was mixed with a carbon support by ball

milling for three minutes as well. All RDEs were cleaned by bath sonication in a 50:50 by

volume solution of EtOH and DI water followed by polishing on pad with 50 μm alumina,

rinsing with DI water and finished by sonication in a fresh 50:50 EtOH: DI water solution.

Catalyst inks were prepared by adding 2 mL of NaOH neutralized 0.05 wt% Nafion in ethanol

solution to 2 mg of catalyst (1 mg/ml) and sonicating the ink for 2 hours. 10 μL of the ink was

then pipetted onto a 0.196 cm^2 glassy carbon (GC) rotating disk electrode (RDE) and spun dried

at 700 r.p.m. to give a composite mass loading of 51 $\mu g/cm^2$ for LNO on carbon samples. This

relatively low mass loading was chosen to limit mass transfer limitations in the composite film to

best measure intrinsic catalyst activities[39–41]. 7 µL (35.7 µg/cm^2) of ink was used for samples

with only carbon, except for rotating ring disk electrode (RRDE) measurement where 51 µg/cm^2

was loaded, to better delineate the carbon support contribution to catalytic activity. All RDEs

were tested in a standard three electrode cell at 1600 r.p.m. with a Hg/HgO (1 M KOH) reference

electrode a Au counter electrode, and a film of catalyst on RDE as the working electrode with a

room temperature 0.1 M KOH solution saturated with research grade O$_2$. RRDE and CV

experiments were in identical configurations on the Metrohm Autolab PGSTAT302N except the

solutions were saturated with research grade Ar. The positive feedback method was used to

determine electrolyte resistance (~46.8 Ω). The solution resistance was measured for each clean

RDE used, an average was taken, the differences of the RDE solution resistance were calculated

from the average and the iR correction (Figure S2) was adjusted to account for slight differences

in RDE resistance between electrodes.

All electrochemical tests used a Hg/HgO electrode whose open circuit potential (OCP)

was measured relative to the calibrated Hg/HgO electrode to ensure a potential is never applied

to the calibrated electrode. The RHE calibration procedure is provided in the Supplementary

Information and the RHE potential was found to be -0.8937 V versus the calibrated Hg/HgO

(Figure S3). Linear sweep voltammograms (LSV) were performed on RDEs and were scanned at

10 mV/s and 5 mV/s for the OER and ORR, respectively. The OER test window was between

1.0307 V and 1.9937 V vs RHE, while the ORR test window was between 1.0937 V and -0.0063

V vs RHE. All OER and ORR measurements were taken in triplicate. Cyclic voltammograms

(CVs) were taken on static rotating ring disk electrodes (0.2472 cm^2) at 100 mV/s from 0 to 1.4

V vs RHE in 0.1 M KOH solution saturated with Ar for at least 30 minutes. RRDE tests in the

OER region were performed in identical conditions to the CVs at 10 mV/s with the Pt ring

(0.1859 cm^2) cycled in the ORR region to reduce surface oxides and held at 0.5V vs RHE. The

ORR RRDE measurements were performed at the same conditions as the ORR RDE

measurements with the Pt ring held at 1.23 V vs RHE to ensure all ring current was due to

peroxide oxidation. The collection efficiency was previously measured to be 37%[19] using 0.3

mM ferrocene-methanol in 0.1 M KCl by sweeping the disk potential from 0.1 V to 0.6 V vs

Hg/HgO and holding the Pt ring potential at 0.1 V vs Hg/HgO.

Samples for ICP-OES were made by taking 4.55 mL of the electrolyte before OER CVs

(sample "KOH"), after one OER CV on a carbon fiber paper (CFP) electrode (sample "CFP")

and following a OER CV of 0.3 mg cm^{-2} N-CNT on a CFP electrode (sample "N-CNT"). The

CFP working electrodes were attached to a copper wire using copper tape to avoid iron

contamination in the solution. Before ICP-OES measurements, 0.45 mL of 12.1 M trace metal

nitric acid was added to the electrolyte samples to bring the solution to 2 wt% nitric acid.

Results and Discussion

Characterization: Carbon Nanotubes and LNO

The N-CNT and CNT samples were well characterized before mixing with LNO to more

fully understand the role of the carbon support towards OER and ORR. Figure 1a shows a

representative high resolution TEM image of N-CNTs ranging from 5 to 20 nm in diameter.

Additionally, the Fe nanoparticles (NPs) shown in the TEM and HAADF-STEM images of

Figure S4 are approximately 10-20 nm in diameter and are encased in graphitic shells that are ca.

3-8 atomic layers thick. EDX (Figure S5) and EELS (Figure S6) spectra show that the N-CNT

sample is composed of mostly C and Fe. EELS spectra display a small nitrogen signal around

410 eV.

XRD, a bulk technique, was used to determine the size of graphitic domains using the

Scherrer equation (5.3 nm and 10.4 nm for N-CNTs and CNTs, respectively) along with the

crystal structure of the Fe catalyst in the N-CNT and CNT samples. Figure S7a shows the
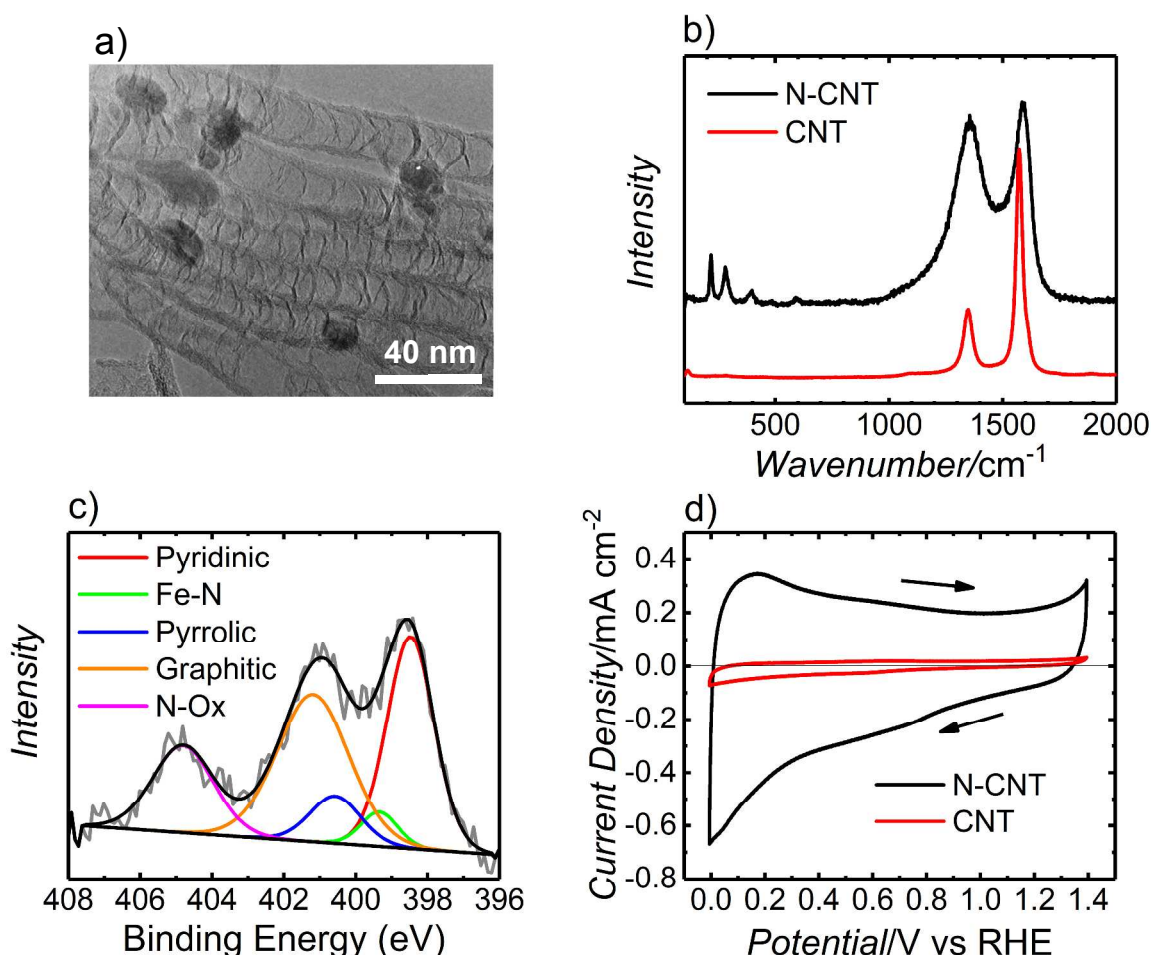
Figure 1. a) TEM images showing N-CNTs with encapsulated Fe nanoparticles b) Normalized

Raman spectra of both N-CNTs and CNTs c) High resolution XPS spectra of N 1s of N-CNTs

d) CVs of N-CNTs and CNTs in Ar saturated 0.1 M KOH at 100 mV/s with 51 μg/cm^2 total

mass loading.

normalized XRD spectra of both samples each with two peaks, the first at 26° and the second at

44.5^o 2θ corresponding to graphite and iron carbide (Fe$_3$C), respectively. The LNO was found to

be phase pure as shown in Figure S7b.

TGA was used to determine the total iron content in the two samples (Figure S8). The residual iron after thermal decomposition was found to be Fe_2O_3 using XRD which was weighed and its mass converted to what it would be if it were Fe_3C giving a weight percent for N-CNTs and CNTs of 20.6 wt. % and 11.9 wt. %, respectively. The N-CNT burn off temperature appears to be 400^oC, and that of the CNTs is approximately 550^oC indicating the latter's greater thermal stability.

Raman spectra of N-CNTs in Figure 1b show that the N-CNTs are much more disordered than CNTs as can be seen by the relative intensities of the two peaks at approximately 1360 cm^{-1} and 1590 cm^{-1} which are commonly referred to as the D and G bands, respectively. The D band is attributed to the A_{1g} vibrational mode which is normally not Raman active, but becomes active when translational symmetry is broken in graphitic planes[42]. This broken symmetry occurs at graphite plane edges, vacancies, functionalities or any non-graphite bond[43]. The G band is assigned to the E_{2g} vibrational mode corresponding to in-plane sp^2 graphitic carbon. Tunistra *et. al.* showed[43] that the average graphite crystal size is inversely proportional to the I_D/I_G ratio which was found to be 0.91, 0.31, and 1.94[44] for the N-CNTs, CNTs and VC, respectively, giving average graphite crystallite sizes of 4.8, 10.3, 2.2 nm for the respective carbons. The smaller N-CNT graphite domain size relative to the CNTs makes intuitive sense as N-dopants would break the graphite translational symmetry and would manifest as a larger D band. The collection of peaks below 600 cm^{-1} for the N-CNTs correspond to α-Fe_2O_3 (hematite)[45,46] which is not detected in the bulk from XRD, thus suggesting that the Fe_3C particles in N-CNTs are coated in a thin α-Fe_2O_3 layer. The presence of hematite peaks in the N-CNT sample suggest that the N-CNT structure is disordered enough to allow access to oxygen from the air to oxidize the Fe_3C in the sample at ambient conditions. In contrast, CNTs do not show hematite Raman active

bands thus suggesting that the iron carbide nanoparticles are completely coated in an impermeable graphite layer since Fe_3C does not have Raman active vibrational modes[46].

XPS spectra were taken on both samples and the total nitrogen content of the N-CNTs was found to be 5.6 ± 0.5 at. %. Significant contributions are computed in Table S2 and shown in Figure 1c from pyridinic nitrogen (398.5 eV), nitrogen coordinated iron (399.3 eV), pyrrolic nitrogen (400.5 eV)[47], graphitic nitrogen (401.2 eV)[47], and pyridine-N-oxide (404.8 eV)[47,48]. Examining the XPS surveys of both samples in Figure S9 reveals that there is no detectable Fe in the CNT sample while there is only 1.02 at.% Fe (~4.8 wt. % Fe_3C) corresponding to roughly one quarter of that detected by TGA. The lower iron content is likely because XPS penetration depth is approximately 10 nm and each Fe NP seed appears to be coated in a ~5 nm graphitic shell. Each nanoparticle is approximately 20 nm in diameter in Figure S4 so the XPS signal would not realistically penetrate the entire sample. Both samples display a small oxygen signal as shown in Figure S10 which is mostly due to FeOOH[49] in the N-CNTs from the decomposition of adsorbed water while the undoped CNTs' spectra reveal adsorbed water and Fe_3O_4[50]. This observation agrees with the N-CNT Raman spectrum and the small size of the O 1s shoulder in the CNT spectra suggests that perhaps there is only slight oxidation of the Fe NP catalyst, possibly due to oxygen diffusion through graphitic edges and grain boundaries.

Ar saturated CVs of both samples, shown in Figure 1d, were taken to quantify possible redox features. N-CNT reduction current begins to increase at ~0.3 V vs RHE which corresponds to a transition of α-Fe_2O_3 to Fe_3O_4 according to the iron Pourbaix diagram in Figure S11[51]. The capacitance of the N-CNTs and CNTs were determined to be 143 F/g and 11 F/g, respectively by using the cathodic scan as shown previously.[9] This increase is due in part to the ~5-fold increase in surface area of N-CNTs (200 m^2/g) relative to CNTs (46 m^2/g) as shown in Figure S12.

Wiggins-Camacho *et.al.*[52]explained the remainder of the 13-fold increase in capacitance from nitrogen doping as a result of a higher density of states at the Fermi level that increases the capacitance per unit area. Additionally, Rice *et. al.*[53] have shown that edge plane carbon has a significantly higher capacitance per unit area than its basal plane counterpart. This observation also helps to explain the higher capacitance of N-CNTs due to their higher edge plane content according to their Raman spectra in Figure 1b.

Oxygen Reduction Reaction

Figure 2a shows the ORR activity of VC, CNT, and N-CNT supports with and without LNO as shown by the solid and dashed lines, respectively. All RDEs are loaded with 35.7 $\mu g/cm^2$ of carbon and an additional 15.3 $\mu g/cm^2$ of LNO. In all cases adding LNO (solid lines) raised the reduction current. For the 'carbon only' curves, the onset potential and diffusion limited current increases in the order CNT < VC < N-CNT. The low diffusion limited current of VC and the CNTs suggests that only the first two electrons are transferred to O_2 to form HO_2^- (eqn. 2) on the carbon which was confirmed by the RRDE measurements in Figure S13 where all of the measured disk current was due to peroxide generation until ~0.2V vs RHE where peroxide electroreduction (eqn. 3) begins to take place. The low CNT activity can be explained from the fact that it has many fewer edge sites and defects according to the Raman spectra, features that are known to produce much higher electron transfer rates[54]. VC, in contrast, has more defects as well as a slight sulfur content[44] that has been shown to increase ORR activity[55]. The N-CNTs have significantly more defects, and more importantly, they have 5.6 ± 0.5 at% N dopants which are well known to catalyze the ORR while the residual Fe or its oxides can chemically disproportionate peroxide[17] thus yielding the pseudo four electron mechanistic pathway.[13,17,37,56]
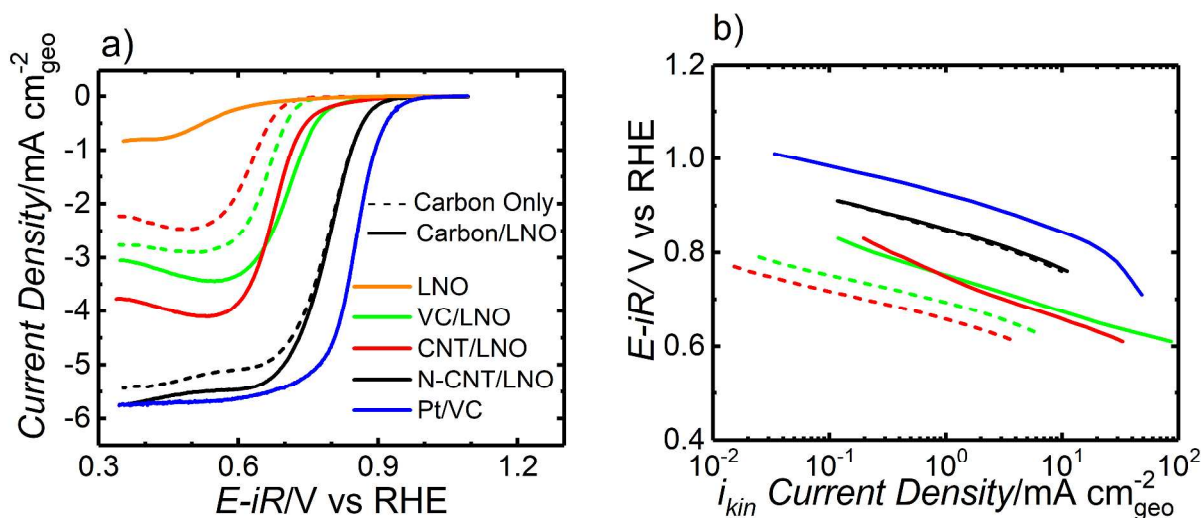
Figure 2. ORR in O_2-saturated 0.1 M KOH at 1600 r.p.m. and a 51 μg/cm^2 mass loading a) Activity b) Tafel plot of the kinetic current obtained from the Koutecky-Levich equation (eqn. S4). The dashed lines correspond to the carbon only (35.7 μg/cm^2) and the solid lines correspond to the LNO-carbon composite while the orange 'LNO' solid line represent LNO (15.3 μg/cm^2) without carbon. Note that adding LNO and doping N into CNTs increases the diffusion limited current as well as the exchange current density indicated by the shift of the curves to higher potentials. All Tafel curves are the average of three RDE experiments.

There has been much debate about the nature of the active site from doping carbon with N. For example, the carbon atoms straddling both sides of edge sites containing pyridinic nitrogen atoms have been shown to be the ORR active site in both acidic[57] and neutral[17] conditions. In alkaline conditions however, carbon atoms adjacent to graphitic nitrogen are thought to act as the active site for the ORR while carbon atoms neighboring pyridinic nitrogen atoms are supposedly active toward the OER.[58]. Regardless of the identity of the ORR active site, N dopants are known to lower the ORR overpotential by donating electron density to the carbon lattice, thereby raising the Fermi level[52,59] and enhancing the affinity to donate electrons

to solution according to Gerischer-Marcus theory[60]. This increase in the density of states at the Fermi level[52] also increases charge transfer rates and decreases the ORR overpotential which has been experimentally verified by Cheon *et.al*[61]. Taking Gerischer-Marcus theory into account, the finding by Yang *et.al.*[58] is somewhat unusual, because pyridinic N has a lower binding energy than graphitic N so one would expect carbons adjacent to pyridinic N to have more reducing power and thus to be more active towards the ORR. The higher diffusion limited current, however, is likely because the residual Fe in the N-CNTs chemically disproportionates the hydroperoxide formed by the carbon as shown previously via the pseudo-four electron process [17]. The RRDE measurement performed on N-CNTs shown in Figure S13e confirms that the N-CNTs follow the pseudo-four electron process alone at lower overpotentials until ~0.5 V vs RHE, after which it is then accompanied by peroxide electroreduction. The Pt ring current magnitude rises but then falls instead of plateauing (along with the disk current) as it should if it is chemically limited by peroxide disproportionation.

Interestingly, supporting LNO on carbon shifts the onset potential to approximately the same potential for the VC and CNT composite, despite LNO exhibiting little ORR activity itself but does not affect the onset potential for the N-CNTs. Additionally, the order of increasing diffusion limited current with LNO changes to VC < CNT < N-CNT. These observations can be explained from the RRDE measurements in Figure S13 that show adding LNO chemically disproportionates peroxide generated on the cathodic scan which was previously rate limiting. The peroxide generation current increases on the back scan for both VC/LNO and CNT/LNO which suggests LNO peroxide chemical disproportionation activity decreases on the anodic sweep. We examined the reversibility of LNO by doing a second scan on the two composites shown in Figure S14 which shows there is no chemical disproportionation of peroxide for

VC/LNO while it is reduced by half for the CNT/LNO. By looking at the blue difference curves in Figure S14, it appears the LNO electroreduces peroxide (eqn. 3) in VC/LNO where VC did not before, and CNT/LNO has a four-fold increase in the peroxide electroreduction rate relative to CNT alone (Figure S13c). The latter observation may be explained by noting that peroxide electroreduction requires charge transfer and the CNTs will increase the electrical conductivity of the composite relative to LNO, reducing any charge transfer resistances. While, LNO peroxide chemical disproportionation is likely slower than the iron in the N-CNT, it also assists in the chemical disproportionation and electroreduction of hydroperoxide generated on N-CNTs because the composite's current increases uniformly over the entire diffusion limited regime with the LNO addition[11,17].

Later in this paper we demonstrate that the iron inside the N-CNT is anodically leached at OER potentials and we use RRDE measurements to show how the ORR activity changes before and after running an OER CV (Figure S15, S16) . It appears the CNTs have enhanced peroxide electroreduction rates after an OER CV, which is likely due to oxygen functionalities formed during the OER, yet peroxide generation rates remain unchanged. In contrast, Figure S16 more clearly illustrates that the CNT/LNO composite and N-CNTs maintain their electroreduction activity while losing much of their peroxide disproportionation activity after an OER CV. LNO appears to stabilize the N-CNT ORR activity with minimal loss as shown in Figure S15g and h after much of the iron is leached from the support during the OER. A possible explanation for this is as the iron is leached from the N-CNTs, it interacts with LNO to form Ni-Fe species on the surface so there would still be iron present to catalyze the pseudo-four electron mechanism. This hypothesis is supported by the Ni redox peak anodic shift shown in Figure S17a which will be discussed in greater detail later in this paper.

Tafel plots are shown in Figure 2b with measured Tafel slopes reported in Table S3 that are between 60-85 mV/dec. The Tafel slope of approximately 60 mV/dec would be consistent with previous reports that the rate determining step is the protonation of superoxide (reaction S2) according to kinetic modeling studies[62]. This agrees with CV experiments in alkaline conditions at different pH values and scan rates[63], hydroperoxide decomposition measurements and modeling[37], deuterium isotope studies[64] and transfer coefficient analysis[65]. The overpotentials at 3 mA/cm$^2_{geo}$ for N-CNT, CNT and VC composites with LNO are 0.45 V, 0.58 V and 0.59 V, respectively.

Oxygen Evolution Reaction

The geometric OER activity of the different composites is shown in Figure 3a relative to IrO$_2$/VC as a benchmark. While LNO on VC has a higher activity than IrO$_2$ on VC as shown previously[18], the activity rises significantly with the CNT and N-CNT supports. This increase can be explained by the improved electronic conductivity and the high aspect ratio of N-CNTs and CNTs that improve "wiring" of the LNO relative to VC. The conductivities of N-CNT and CNT supports were previously reported[52] to be ~300 $\pm$ 100 and 330 $\pm$ 70 S/cm, respectively, while that of VC is only ~ 5 S/cm[44]. These results explain the difference of the OER curves from VC to N-CNT and CNT supports. The change in the OER i-V curves before and after iR correction, as shown in Figure S2, is similar to the difference in the OER profiles (Fig. 3a) between VC/LNO and CNT/LNO in that they have the same onset potential for the OER yet the CNT/LNO and N-CNT/LNO samples have a much steeper slope which suggests that the higher electronic conductivity of the catalyst-carbon composite is what enhances the LNO OER activity and not a change in the electronic structure of the catalyst.   Tafel plots of the OER activities of the LNO-carbon composites are shown in Figure 3b. For all samples, there are distinct regions

with different Tafel slopes at both low and high overpotentials along with features attributed to

LNO redox reactions[9,66] around the transition between the two regimes at ~1.5 V vs RHE. The
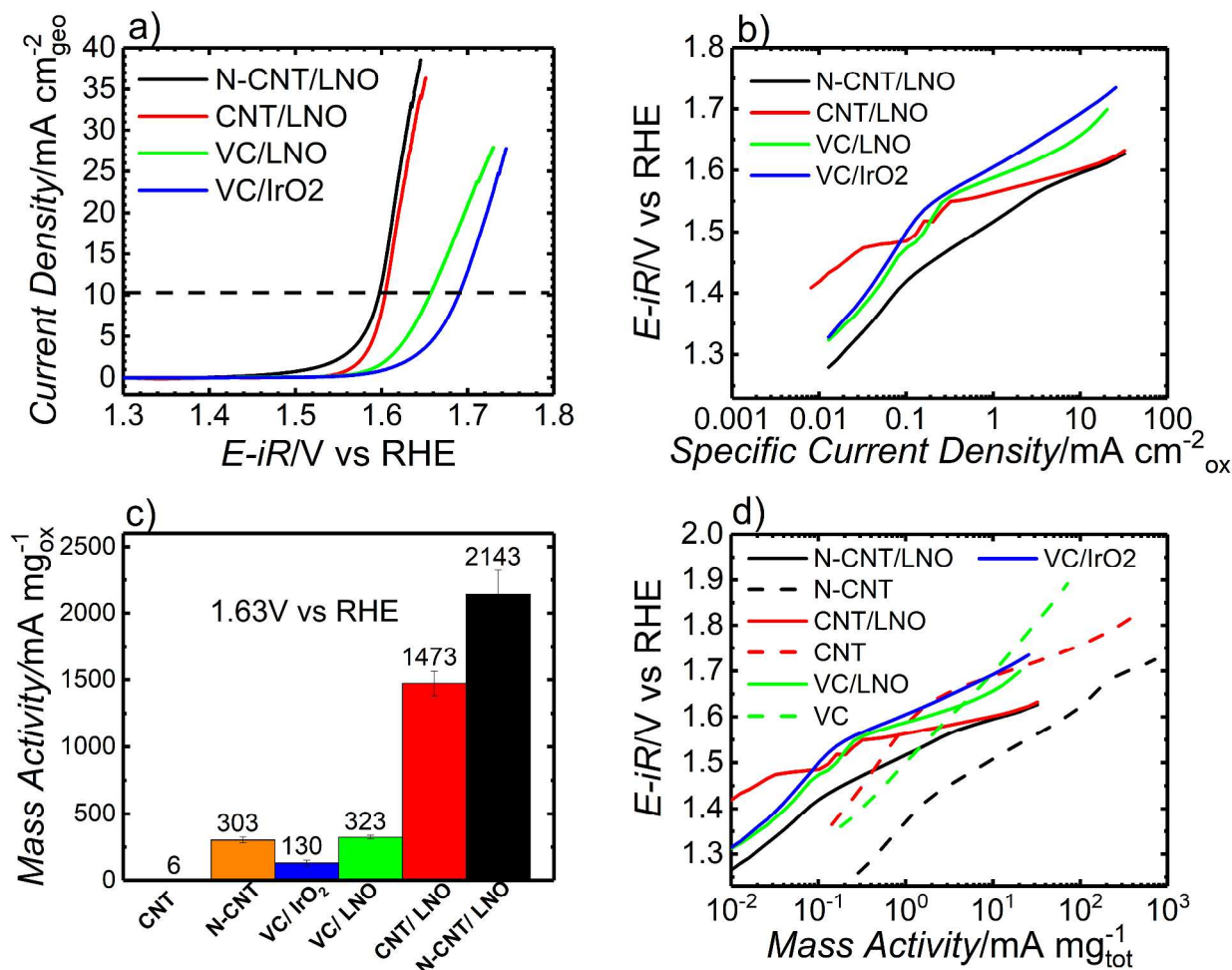
Figure 3. a) Linear and b) log scale plots of OER activities comparing the effects of the

carbon support and performance relative to 30 wt% IrO_2 on VC c) Oxide mass activity

measured at 1.63 V vs. RHE in 0.1 M KOH O_2 saturated solution at 10 mV/s of LNO on

different supports, the carbon supports alone, and VC/IrO_2 benchmark at 51 μg/cm^2 mass

loading. The support activities are normalized to their own mass (35.7 μg/cm^2) d) Total mass

activity of same samples as in c) to better compare the intrinsic role of the support.

N-CNT composite appears to have an intermediate Tafel region between ~1.42-1.57 V vs RHE

which can be more easily seen in Figure S18 where the Tafel slope is plotted for the four

composites vs. log(mass activity).

Table 1: Comparison of Bifunctional Composites					
Sample	**η_{ORR} (V)** -3 mA/cm$^2_{geo}$	**η_{OER} (V)** 10 mA/cm$^2_{geo}$	**ΔE (V)**	**Loading (μg/cm^2)**	**Source**
N-CNT/LNO	0.44	0.37	0.81	51	This work
VC/LNO	0.61	0.42	1.03	51	This work
SP/ Cubic LaNiO$_3$	0.57	0.46	1.04	317	[67]
N-CNT @ LaNiO$_3$	0.46	0.51	0.97	1220	[68]
RGO/ LaNiO$_3$ Nanorod	0.62	0.46	1.08	254	[69]
N-meso C /LaNiO$_3$	0.52	0.43	0.95	51	[11]
Graphene Ox./ LaNiO$_3$	0.604	0.51	1.11	51	[11]
LaNiO$_3$/NC	0.59	0.43	1.02	51	[18]
20% Ir/VC	0.54	0.38	0.92	140	1
20% Pt/VC	0.37	0.79	1.16	140	1

Figure 3c shows the OER activity of LNO on different supports benchmarked against

IrO$_2$/VC and our previous work[11,19] at 1.63 V vs RHE. It demonstrates that the OER activity of

LNO supported on CNTs and N-CNTs is more than 10x and 16x higher, respectively, than

precious metal IrO$_2$ supported on VC. The N-CNT and CNT support activities are normalized by

the total mass of carbon on the electrode (7 μg) and are significantly less active than the metal

oxides. Thus, the carbon support boosts the OER activity of LNO as opposed to catalyzing the

OER itself. The total mass activities are plotted in Figure 3d to better compare the activities of

the carbon support with and without LNO.

While the conductivity of the carbon support can be used to explain the enhanced

activities of CNT/LNO and N-CNT/LNO relative to VC/LNO, one would expect CNT/LNO to

be more active than N-CNT/LNO due to CNT's higher electronic conductivity. The larger

activity enhancement due to N-CNT could possibly be explained by the N-CNTs faster charge

transfer rates. The N-CNTs have a higher density of states at the Fermi level[52] which should raise

charge transfer rates according to Gerisher-Marcus Theory[60] and thus result in higher activities.

The combination of the above effects of N-CNTs and LNO on the ORR and OER enable the

LNO bifunctional window for OER and ORR to drop from 1.03 V on VC to 0.81V on N-CNTs,

which is even lower than the value for the benchmark Ir/VC at three times the loading of N-

CNT/LNO, as shown in Table 1. In fact, the reported N-CNTs here are the most synergistic

resulting in the lowest bifunctional window compared to many other carbon-$LaNiO_3$ composites

with higher mass loadings as shown in Table 1.

Additionally, the carbon's effect on the LNO redox peak is illustrated in Figure S17 by

subtracting the carbon current contribution from the LNO-carbon composite's current to yield

only the contribution due to LNO. Figure S17a shows that, relative to VC, CNTs as a support

raises the redox peak current of LNO 7-fold, while N-CNTs approximately double the peak

height and shift the peaks anodically by ~40 mV. The larger LNO redox peaks are likely due to

the higher electrical conductivity of the carbon nanotubes that enable better utilization of the

LNO surface.

RRDE Carbon Oxidation Studies

Carbon oxidation is always a concern because carbon is thermodynamically unstable[70] at OER

potentials, but the kinetics may become slow enough for highly graphitic carbon to achieve

acceptable catalyst stability[26,29]. A RRDE was submerged into an Ar-saturated 0.1 M KOH

solution and surface oxides were reduced on the Pt ring by cycling the ring at ORR potentials

prior to the test until the CVs stabilized. The Pt ring was held at 0.5 V vs. RHE which is low

enough reduce evolved oxygen, but not any carbon dioxide produced from the carbon on the disc
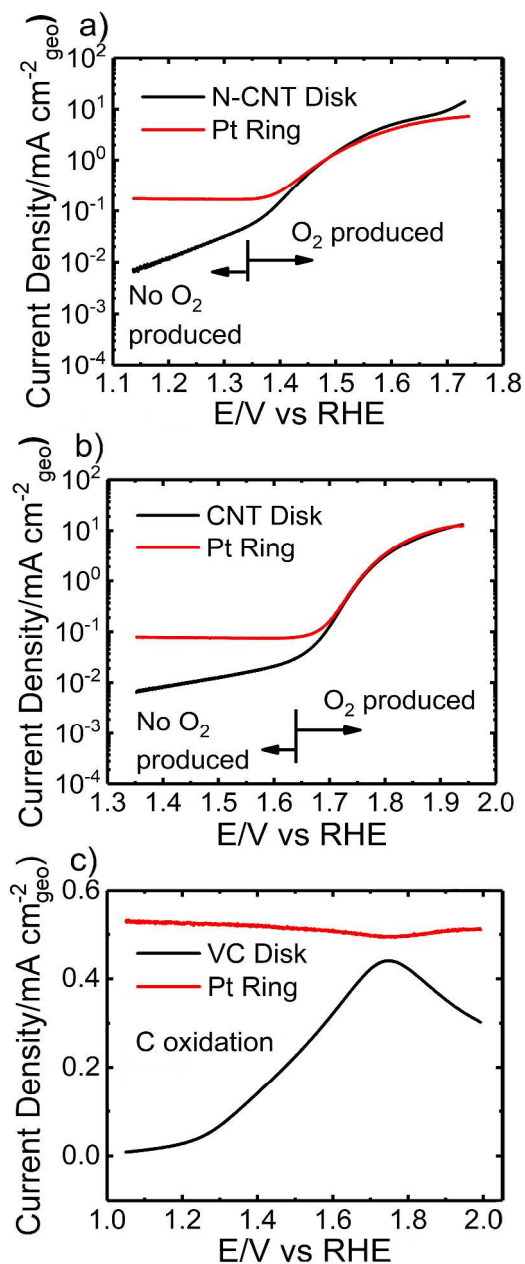
Figure 4. RRDE measurements in Ar saturated 0.1 M KOH at 1600 r.p.m. with 51 μg cm^{-2} mass loading of a) N-CNT b) CNT c) VC. Note that the Pt ring reduction current begins at ~1.35 V and ~1.65V vs RHE for N-CNTs and CNTs, respectively and that the Pt ring background current is higher than the VC oxidation current. All Pt ring currents were divided by the collection efficiency (37%) to demonstrate that anodic disk current is entirely OER as seen by curve overlap.

(Figure 4). The onset potentials for reduction of evolved O_2 at the Pt ring are ~1.37 V and ~1.62

V vs RHE on the disk for N-CNT and CNT (without any LNO) samples, respectively, as shown

in Figure 4. Below these potentials only Pt ring background current is detected and both N-CNTs

and CNTs have a single slope on a log(i) plot indicating a Tafel region with faradaic

charge transfer. Thus, the current measured in this low overpotential region *must* be due to

carbon oxidation because it is the only species present that can be oxidized at this potential

consistent with carbon[70] and iron[51] Pourbaix diagrams.

Speculatively, the reason for the early onset of the Pt ring current for N-CNT supports

may be due to electrochemical leaching of residual Fe which occurs around 1.4 V vs RHE

according to the Fe Pourbaix diagram in Figure S11[51,71]. This result agrees with the Raman and

XPS data that N-CNTs contain both Fe_3C and FeOx that are accessible to the environment.

Further evidence for anodic Fe leaching is seen by presence of a hysteresis loop, as shown in

Figure S19 for N-CNTs in the OER, which rapidly shrinks in intensity after the first scan as the

iron is removed. Additionally, ICP-OES measurements show, in Figure S20, that iron is present

in the electrolyte after CVs of the N-CNT sample in the OER region to confirm Fe leaching. The

RRDE experiment with VC (Figure 4c) shows that no oxygen was evolved and that there was so

little current that the Pt ring background current was always higher than the VC disk current.

This result demonstrates that VC does not catalyze the OER and that the current is predominately

a result of carbon oxidation.

Whereas the role of carbon oxidation in the OER has often not been quantified in the

literature, in this study we quantitatively separate the effects of carbon oxidation, the OER and

anodic iron leaching. Figure S21 demonstrates that carbon oxidation rates can be extrapolated

from the Tafel slopes in the low overpotential carbon oxidation region assuming the Tafel slope

does not change appreciably with potential. Contributions from anodic iron leaching are quantified by comparing composites with and without LNO and it was found that iron leaching accounted for ~13% of the N-CNT/LNO OER current at 1.63 V vs RHE, while there was no sign of iron leaching for CNT/LNO or CNTs. A summary of the various current contributions for the three composites are given in Tables S5-7, respectively with Tafel slopes and exchange current densities of carbon oxidation extrapolated to 0.099V vs RHE for the various systems in Table S8. It is observed that LNO and IrO_2 change both the Tafel slope and exchange current density for carbon oxidation according to Table S8, which is, speculatively, due to metal-oxide catalyzed carbon oxidation.

OER Constant Current Stability Test

OER 48-hour constant current stability tests of the N-CNTs (10 A/g_{ox}; 30 µA) and CNTs (10 A/g_{tot}; 100 µA) supports with and without LNO were measured and are shown in Figure 5a. Of the four systems studied, all were stable for the entire 48 hour galvanostatic test, except for N-CNTs without LNO, which failed in less than two hours. The greater stability of CNTs relative to N-CNTs, without LNO, was expected considering the Raman spectra show N-CNTs with higher disorder, more edge sites and more defects with dangling bonds that would make N-CNTs more susceptible to oxidation[29,30] than the CNTs. When LNO is supported on CNTs, the overpotential decreases by approximately 50 mV, which would aid carbon stability even though the CNTs alone were already stable for 48-hours. The addition of LNO increases the N-CNT stability from two hours to up to seven days (Figure 5b) since LNO lowers the overpotential for the OER reaction, thereby lowering the carbon oxidation rate. Interestingly, LNO adds a small 'potential rebound' to CNTs (shown in Fig. 5a inset) and N-CNTs. The first overpotential rebound for the CNT/LNO composite is probably due to the LNO redox peak from the

incorporation of solution phase hydroxide[9]. The N-CNT/LNO composite's overpotential kept
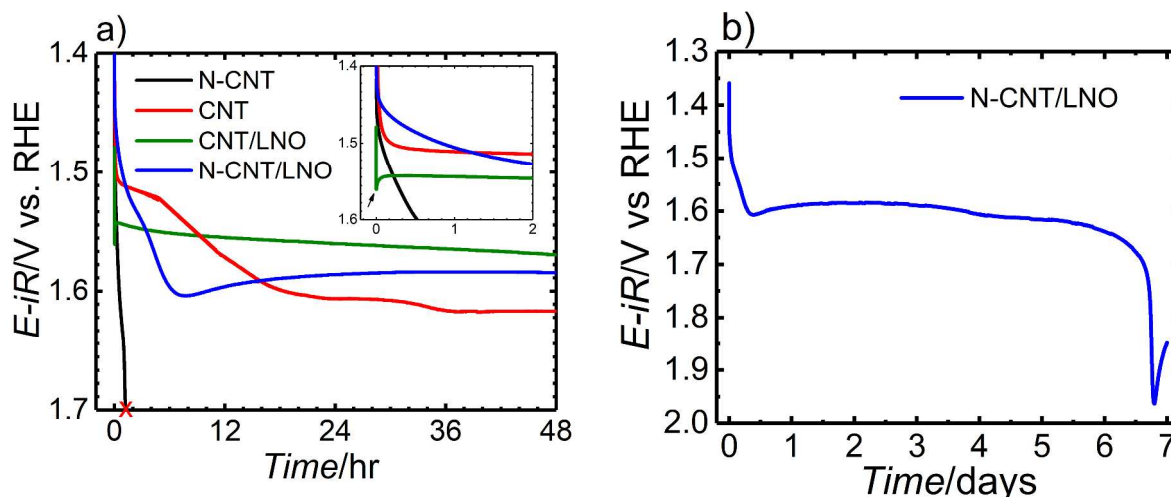
Figure 5. a) 48-hour OER constant current stability test of N-CNTs and CNTs with and

without LNO. N-CNT and N-CNT/LNO are tested at 10 A/g_{ox} (30 μA). CNT and

CNT/LNO are tested at 10A/g_{tot} (100 μA). b) N-CNT/LNO seven-day stability test at same

conditions as in a).

increasing until after eight hours when it decreased and stabilized, which is likely due to a

combination of the LNO redox peak and electrochemical Fe leaching from N-CNTs to a soluble

FeO_4^{2-} as described previously[72]. So far, it is unknown why there exists a second potential

rebound at approximately seven days for the N-CNT/LNO composite. The majority of the

galvanostatic current is likely from the OER catalyzed by LNO because estimates of the carbon

oxidation rate indicate that if all the N-CNT/LNO current were carbon oxidation then it should

have failed after two hours. This estimate is consistent with the stability measurement of N-

CNTs without LNO. Thus, adding an active OER catalyst such as LNO can significantly

suppress carbon oxidation processes via reducing the OER overpotential and therefore the carbon

oxidation overpotential as well.

Conclusions

In summary, we have synthesized CNTs with high nitrogen content using a high yield synthesis, the product of which is the best carbon support to the knowledge of the authors for perovskite oxides as a bifunctional catalyst towards the oxygen evolution and reduction reaction. We compare the N-CNTs with undoped CNTs and Vulcan Carbon to investigate chemical and morphological differences on the impact of activity and stability. The bifunctional window of the N-CNT/LNO composite was measured to be 0.81 V with a mass loading of only 51 µg cm^{-2} that survived over seven days at a constant oxidizing current of 10 A g$_{ox}^{-1}$, which is a much lower mass loading (Table 1) and much longer stability test relative to one-day galvanostatic tests commonly done in the literature. The N-CNT stability was increased from two hours to over seven days by adding LNO which lowered the overpotential and thus rate of carbon oxidation. The high aspect ratio of the more conductive nanotubes enhances electrical wiring between the carbon and catalyst to boost the nanoscale LNO OER activity, while the N-dopants on the carbon along with residual iron catalyze the ORR using "pseudo"-four-electron pathway[17]. We also demonstrate a method to easily use RRDE combined with ICP-OES and Tafel slope analysis to quantitatively identify carbon and iron corrosion *in-situ* to more accurately measure OER activities. This will allow the scientific community to better compare OER catalyst activities and avoid erroneous results from corrosion or comparing catalysts at overpotentials that are too low. The above results demonstrate that the carbon nanotube and LNO systems were rigorously characterized and show promise, upon further optimization, towards being bifunctional composites for metal-air batteries and regenerative fuel cell applications in the future.

ASSOCIATED CONTENT

Supporting Information.

Additional information regarding descriptions of the ORR mechanism, RHE measurement, the Koutecký-Levich equation, CNT furnace configuration, iR correction, RHE measurement, TEM, EDX, EELS, XRD, TGA, XPS, Fe Pourbaix diagram, BET and Tafel slope analysis. This material is available free of charge *via* the Internet at http://pubs.acs.org.

AUTHOR INFORMATION

Corresponding Author

*Keith J. Stevenson (email: k.stevenson@skoltech.ru)

Author Contributions

C.T.A. performed sample synthesis, XRD, XPS, Raman, TGA, BET and electrochemical data collection and analysis. A.A. performed all the high-resolution TEM and HAADF-STEM, EDX, and EELS. R.P.F. assisted in sample synthesis. K.J.S. and K.P.J. assisted in data analysis and constructing the paper.

Funding Sources

Notes

The authors declare no competing financial interest.

ACKNOWLEDGMENT

ABBREVIATIONS

LNO, LaNiO$_3$; CNT, carbon nanotube; N-CNT, nitrogen doped carbon nanotube; VC, Vulcan carbon

REFERENCES

(1)   Vazquez, S.; Lukic, S. M.; Galvan, E.; Franquelo, L. G.; Carrasco, J. M. Energy Storage Systems for Transport and Grid Applications. *IEEE Trans. Ind. Electron.* **2010**, *57* (12), 3881–3895.

(2)   Christensen, J.; Albertus, P.; Sanchez-Carrera, R. S.; Lohmann, T.; Kozinsky, B.; Liedtke, R.; Ahmed, J.; Kojic, A. A Critical Review of Li/Air Batteries. *J. Electrochem. Soc.* **2011**, *159* (2), R1–R30.

(3)   Rahman, M. A.; Wang, X.; Wen, C. High Energy Density Metal-Air Batteries: A Review. *J. Electrochem. Soc.* **2013**, *160* (10), A1759–A1771.

(4)   Gorlin, Y.; Jaramillo, T. F. A Bifunctional Nonprecious Metal Catalyst for Oxygen Reduction and Water Oxidation. *J. Am. Chem. Soc.* **2010**, *132* (39), 13612–13614.

(5)   Hwang, J.; Rao, R. R.; Giordano, L.; Katayama, Y.; Yu, Y.; Shao-Horn, Y. Perovskites in Catalysis and Electrocatalysis. *Science* **2017**, *358* (6364), 751–756.

(6)   Chen, D.; Chen, C.; Baiyee, Z. M.; Shao, Z.; Ciucci, F. Nonstoichiometric Oxides as Low-Cost and Highly-Efficient Oxygen Reduction/Evolution Catalysts for Low-Temperature Electrochemical Devices. *Chem. Rev.* **2015**, *115* (18), 9869–9921.

(7)   Suntivich, J.; May, K. J.; Gasteiger, H. A.; Goodenough, J. B.; Shao-Horn, Y. A Perovskite Oxide Optimized for Oxygen Evolution Catalysis from Molecular Orbital Principles. *Science* **2011**, *334* (6061), 1383–1385.

(8)   Bockris, J. O.; Otagawa, T. The Electrocatalysis of Oxygen Evolution on Perovskites. *J. Electrochem. Soc.* **1984**, *131* (2), 290–302.

(9)   Mefford, J. T.; Hardin, W. G.; Dai, S.; Johnston, K. P.; Stevenson, K. J. Anion Charge Storage through Oxygen Intercalation in LaMnO3 Perovskite Pseudocapacitor Electrodes. *Nat. Mater.* **2014**, *13* (7), 726–732.

(10)   Nemudry, A.; Rudolf, P.; Schöllhorn, R. Topotactic Electrochemical Redox Reactions of the Defect Perovskite SrCoO2.5+x. *Chem. Mater.* **1996**, *8* (9), 2232–2238.

(11)   Hardin, W. G.; Mefford, J. T.; Slanac, D. A.; Patel, B. B.; Wang, X.; Dai, S.; Zhao, X.; Ruoff, R. S.; Johnston, K. P.; Stevenson, K. J. Tuning the Electrocatalytic Activity of Perovskites through Active Site Variation and Support Interactions. *Chem. Mater.* **2014**, *26* (11), 3368–3376.

(12) Suntivich, J.; Gasteiger, H. A.; Yabuuchi, N.; Nakanishi, H.; Goodenough, J. B.; Shao-Horn, Y. Design Principles for Oxygen-Reduction Activity on Perovskite Oxide Catalysts for Fuel Cells and Metal–air Batteries. *Nat. Chem.* **2011**, *3* (7), 546–550.

(13) Gong, K.; Du, F.; Xia, Z.; Durstock, M.; Dai, L. Nitrogen-Doped Carbon Nanotube Arrays with High Electrocatalytic Activity for Oxygen Reduction. *Science* **2009**, *323* (5915), 760–764.

(14) Zhou, M.; Wang, H.-L.; Guo, S. Towards High-Efficiency Nanoelectrocatalysts for Oxygen Reduction through Engineering Advanced Carbon Nanomaterials. *Chem. Soc. Rev.* **2016**, *45* (5), 1273–1307.

(15) Yeager, E. Electrocatalysts for O2 Reduction. *Electrochimica Acta* **1984**, *29* (11), 1527–1537.

(16) Poux, T.; Napolskiy, F. S.; Dintzer, T.; Kéranguéven, G.; Istomin, S. Y.; Tsirlina, G. A.; Antipov, E. V.; Savinova, E. R. Dual Role of Carbon in the Catalytic Layers of Perovskite/Carbon Composites for the Electrocatalytic Oxygen Reduction Reaction. *Catal. Today* **2012**, *189* (1), 83–92.

(17) Wiggins-Camacho, J. D.; Stevenson, K. J. Mechanistic Discussion of the Oxygen Reduction Reaction at Nitrogen-Doped Carbon Nanotubes. *J. Phys. Chem. C* **2011**, *115* (40), 20002–20010.

(18) Hardin, W. G.; Slanac, D. A.; Wang, X.; Dai, S.; Johnston, K. P.; Stevenson, K. J. Highly Active, Nonprecious Metal Perovskite Electrocatalysts for Bifunctional Metal–Air Battery Electrodes. *J. Phys. Chem. Lett.* **2013**, *4* (8), 1254–1259.

(19) Mefford, J. T.; Rong, X.; Abakumov, A. M.; Hardin, W. G.; Dai, S.; Kolpak, A. M.; Johnston, K. P.; Stevenson, K. J. Water Electrolysis on La1-XSrxCoO3-δ Perovskite Electrocatalysts. *Nat. Commun.* **2016**, *7*, 11053.

(20) Seitz, L. C.; Dickens, C. F.; Nishio, K.; Hikita, Y.; Montoya, J.; Doyle, A.; Kirk, C.; Vojvodic, A.; Hwang, H. Y.; Norskov, J. K.; Jaramillo, T.K. A Highly Active and Stable IrOx/SrIrO3 Catalyst for the Oxygen Evolution Reaction. *Science* **2016**, *353* (6303), 1011–1014.

(21) Rong, X.; Parolin, J.; Kolpak, A. M. A Fundamental Relationship between Reaction Mechanism and Stability in Metal Oxide Catalysts for Oxygen Evolution. *ACS Catal.* **2016**, *6* (2), 1153–1158.

(22) Grimaud, A.; Diaz-Morales, O.; Han, B.; Hong, W. T.; Lee, Y.-L.; Giordano, L.; Stoerzinger, K. A.; Koper, M. T. M.; Shao-Horn, Y. Activating Lattice Oxygen Redox Reactions in Metal Oxides to Catalyse Oxygen Evolution. *Nat. Chem.* **2017**, *9*, 457.

(23) Jung, J.-I.; Risch, M.; Park, S.; Kim, M. G.; Nam, G.; Jeong, H.-Y.; Shao-Horn, Y.; Cho, J. Optimizing Nanoparticle Perovskite for Bifunctional Oxygen Electrocatalysis. *Energy Env. Sci* **2016**.

(24) Lee, D. U.; Park, M. G.; Park, H. W.; Seo, M. H.; Ismayilov, V.; Ahmed, R.; Chen, Z. Highly Active Co-Doped LaMnO 3 Perovskite Oxide and N-Doped Carbon Nanotube Hybrid Bi-Functional Catalyst for Rechargeable Zinc–air Batteries. *Electrochem. Commun.* **2015**, *60*, 38–41.

(25) Elumeeva, K.; Masa, J.; Sierau, J.; Tietz, F.; Muhler, M.; Schuhmann, W. Perovskite-Based Bifunctional Electrocatalysts for Oxygen Evolution and Oxygen Reduction in Alkaline Electrolytes. *Electrochimica Acta* **2016**, *208*, 25–32.

(26) Elumeeva, K.; Masa, J.; Tietz, F.; Yang, F.; Xia, W.; Muhler, M.; Schuhmann, W. A Simple Approach towards High-Performance Perovskite-Based Bifunctional Oxygen Electrocatalysts. *ChemElectroChem* **2016**, *3* (1), 138–143.

(24) Zhu, Y.; Zhou, W.; Shao, Z. Perovskite/Carbon Composites: Applications in Oxygen Electrocatalysis. *small* **2017,** 13 (12)n/a-n/a.

(28) Liu, J.; Jin, X.; Song, W.; Wang, F.; Wang, N.; Song, Y. Facile Preparation of Modified Carbon Black-LaMnO3 Hybrids and the Effect of Covalent Coupling on the Catalytic Activity for Oxygen Reduction Reaction. *Chin. J. Catal.* **2014**, *35* (7), 1173–1188.

(29) Yu, P. T.; Gu, W.; Makharia, R.; Wagner, F. T.; Gasteiger, H. A. The Impact of Carbon Stability on PEM Fuel Cell Startup and Shutdown Voltage Degradation. *ECS Trans.* **2006**, *3* (1), 797–809.

(30) Datsyuk, V.; Kalyva, M.; Papagelis, K.; Parthenios, J.; Tasis, D.; Siokou, A.; Kallitsis, I.; Galiotis, C. Chemical Oxidation of Multiwalled Carbon Nanotubes. *Carbon* **2008**, *46* (6), 833–840.

(31) Soares, C. O.; Silva, R. A.; Carvalho, M. D.; Jorge, M. E. M.; Gomes, A.; Rangel, C. M.; da Silva Pereira, M. I. Oxide Loading Effect on the Electrochemical Performance of LaNiO3 Coatings in Alkaline Media. *Electrochimica Acta* **2013**, *89*, 106–113.

(32) Bauer, A.; Song, C.; Ignaszak, A.; Hui, R.; Zhang, J.; Chevallier, L.; Jones, D.; Rozière, J. Improved Stability of Mesoporous Carbon Fuel Cell Catalyst Support through Incorporation of TiO2. *Electrochimica Acta* **2010**, *55* (28), 8365–8370.

(33) Kim, H. J.; Jackson, D. H. K.; Lee, J.; Guan, Y.; Kuech, T. F.; Huber, G. W. Enhanced Activity and Stability of TiO2-Coated Cobalt/Carbon Catalysts for Electrochemical Water Oxidation. *ACS Catal.* **2015**, *5* (6), 3463–3469.

(34) Maldonado, S.; Morin, S.; Stevenson, K. J. Structure, Composition, and Chemical Reactivity of Carbon Nanotubes by Selective Nitrogen Doping. *Carbon* **2006**, *44* (8), 1429–1437.

(35) McCrory, C. C. L.; Jung, S.; Peters, J. C.; Jaramillo, T. F. Benchmarking Heterogeneous Electrocatalysts for the Oxygen Evolution Reaction. *J. Am. Chem. Soc.* **2013**, *135* (45), 16977–16987.

(36) Singh, C.; Shaffer, M. S.; Windle, A. H. Production of Controlled Architectures of Aligned Carbon Nanotubes by an Injection Chemical Vapour Deposition Method. *Carbon* **2003**, *41* (2), 359–368.

(37) Maldonado, S.; Stevenson, K. J. Influence of Nitrogen Doping on Oxygen Reduction Electrocatalysis at Carbon Nanofiber Electrodes. *J. Phys. Chem. B* **2005**, *109* (10), 4707–4716.

(38) Cushing, B. L.; Kolesnichenko, V. L.; O'Connor, C. J. Recent Advances in the Liquid-Phase Syntheses of Inorganic Nanoparticles. *Chem. Rev.* **2004**, *104* (9), 3893–3946.

(39) Garsany, Y.; Singer, I. L.; Swider-Lyons, K. E. Impact of Film Drying Procedures on RDE Characterization of Pt/VC Electrocatalysts. *J. Electroanal. Chem.* **2011**, *662* (2), 396–406.

(40) Wiberg, G. K. H.; Mayrhofer, K. J. J.; Arenz, M. Investigation of the Oxygen Reduction Activity on Silver – A Rotating Disc Electrode Study. *Fuel Cells* **2010**, *10* (4), 575–581.

(41) Schmidt, T. J.; Gasteiger, H. A.; Stäb, G. D.; Urban, P. M.; Kolb, D. M.; Behm, R. J. Characterization of High□Surface□Area Electrocatalysts Using a Rotating Disk Electrode Configuration. *J. Electrochem. Soc.* **1998**, *145* (7), 2354–2358.

(42)   Wang, Y.; Alsmeyer, D. C.; McCreery, R. L. Raman Spectroscopy of Carbon Materials: Structural Basis of Observed Spectra. *Chem. Mater.* **1990**, *2* (5), 557–563.

(43)   Tuinstra, F.; Koenig, J. L. Characterization of Graphite Fiber Surfaces with Raman Spectroscopy. *J. Compos. Mater.* **1970**, *4* (4), 492–499.

(44)   Pantea, D.; Darmstadt, H.; Kaliaguine, S.; Sümmchen, L.; Roy, C. Electrical Conductivity of Thermal Carbon Blacks: Influence of Surface Chemistry. *Carbon* **2001**, *39* (8), 1147–1158.

(45)   Baratto, C.; Lottici, P. P.; Bersani, D.; Antonioli, G.; Gnappi, G.; Montenero, A. Sol-Gel Preparation of α-Fe2O3 Thin Films: Structural Characterization by XAFS and Raman. *J. Sol-Gel Sci. Technol. 13* (1–3), 667–671.

(46)   Park, E.; Ostrovski, O.; Zhang, J.; Thomson, S.; Howe, R. Characterization of Phases Formed in the Iron Carbide Process by X-Ray Diffraction, Mossbauer, X-Ray Photoelectron Spectroscopy, and Raman Spectroscopy Analyses. *Metall. Mater. Trans. B 32* (5), 839–845.

(47)   Pels, J. R.; Kapteijn, F.; Moulijn, J. A.; Zhu, Q.; Thomas, K. M. Evolution of Nitrogen Functionalities in Carbonaceous Materials during Pyrolysis. *Carbon* **1995**, *33* (11), 1641–1653.

(48)   Biniak, S.; Szymański, G.; Siedlewski, J.; Świtkowski, A. The Characterization of Activated Carbons with Oxygen and Nitrogen Surface Groups. *Carbon* **1997**, *35* (12), 1799–1810.

(49)   Allen, G. C.; Curtis, M. T.; Hooper, A. J.; Tucker, P. M. X-Ray Photoelectron Spectroscopy of Iron–oxygen Systems. *J. Chem. Soc. Dalton Trans.* **1974**, *0* (14), 1525–1530.

(50)   Marcus, P.; Grimal, J. M. The Anodic Dissolution and Passivation of NiCrFe Alloys Studied by ESCA. *Corros. Sci.* **1992**, *33* (5), 805–814.

(51)   Jain, A.; Ong, S. P.; Hautier, G.; Chen, W.; Richards, W. D.; Dacek, S.; Cholia, S.; Gunter, D.; Skinner, D.; Ceder, G.; Persson, K. A. Commentary: The Materials Project: A Materials Genome Approach to Accelerating Materials Innovation. *APL Mater.* **2013**, *1* (1), 011002.

(52)   Wiggins-Camacho, J. D.; Stevenson, K. J. Effect of Nitrogen Concentration on Capacitance, Density of States, Electronic Conductivity, and Morphology of N-Doped Carbon Nanotube Electrodes. *J. Phys. Chem. C* **2009**, *113* (44), 19082–19090.

(53)   Rice, R. J.; McCreery, R. L. Quantitative Relationship between Electron Transfer Rate and Surface Microstructure of Laser-Modified Graphite Electrodes. *Anal. Chem.* **1989**, *61* (15), 1637–1641.

(54)   Cline, K. K.; McDermott, M. T.; McCreery, R. L. Anomalously Slow Electron Transfer at Ordered Graphite Electrodes: Influence of Electronic Factors and Reactive Sites. *J. Phys. Chem.* **1994**, *98* (20), 5314–5319.

(55)   Yang, Z.; Yao, Z.; Li, G.; Fang, G.; Nie, H.; Liu, Z.; Zhou, X.; Chen, X.; Huang, S. Sulfur-Doped Graphene as an Efficient Metal-Free Cathode Catalyst for Oxygen Reduction. *ACS Nano* **2012**, *6* (1), 205–211.

(56)   Dai, L.; Xue, Y.; Qu, L.; Choi, H.-J.; Baek, J.-B. Metal-Free Catalysts for Oxygen Reduction Reaction. *Chem. Rev.* **2015**, *115* (11), 4823–4892.

(57)   Guo, D.; Shibuya, R.; Akiba, C.; Saji, S.; Kondo, T.; Nakamura, J. Active Sites of Nitrogen-Doped Carbon Materials for Oxygen Reduction Reaction Clarified Using Model Catalysts. *Science* **2016**, *351* (6271), 361–365.

(58) Yang, H. B.; Miao, J.; Hung, S.-F.; Chen, J.; Tao, H. B.; Wang, X.; Zhang, L.; Chen, R.; Gao, J.; Chen, H. M.; Dai, L.; Liu, B. Identification of Catalytic Sites for Oxygen Reduction and Oxygen Evolution in N-Doped Graphene Materials: Development of Highly Efficient Metal-Free Bifunctional Electrocatalyst. *Sci. Adv.* **2016**, *2* (4), e1501122.

(59) Terrones, M.; Ajayan, P. M.; Banhart, F.; Blase, X.; Carroll, D. L.; Charlier, J. C.; Czerw, R.; Foley, B.; Grobert, N.; Kamalakaran, R.; Kohler-Redlich, P.; Rühle, M.; Seeger, T.; Terrones, H. N-Doping and Coalescence of Carbon Nanotubes: Synthesis and Electronic Properties. *Appl. Phys. A* **2002**, *74* (3), 355–361.

(60) Bard, A. J. *Electroanalytical Chemistry: A Series of Advances:*; CRC Press, 1990.

(61) Cheon, J. Y.; Kim, J. H.; Kim, J. H.; Goddeti, K. C.; Park, J. Y.; Joo, S. H. Intrinsic Relationship between Enhanced Oxygen Reduction Reaction Activity and Nanoscale Work Function of Doped Carbons. *J. Am. Chem. Soc.* **2014**, *136* (25), 8875–8878.

(62) Shinagawa, T.; Garcia-Esparza, A. T.; Takanabe, K. Insight on Tafel Slopes from a Microkinetic Analysis of Aqueous Electrocatalysis for Energy Conversion. *Sci. Rep.* **2015**, *5*, 13801.

(63) Yang, H.-H.; McCreery, R. L. Elucidation of the Mechanism of Dioxygen Reduction on Metal□Free Carbon Electrodes. *J. Electrochem. Soc.* **2000**, *147* (9), 3420–3428.

(64) Xu, J.; Huang, W.; McCreery, R. L. Isotope and Surface Preparation Effects on Alkaline Dioxygen Reduction at Carbon Electrodes. *J. Electroanal. Chem.* **1996**, *410* (2), 235–242.

(65) Maldonado, S.; Stevenson, K. J. Direct Preparation of Carbon Nanofiber Electrodes via Pyrolysis of Iron(II) Phthalocyanine: Electrocatalytic Aspects for Oxygen Reduction. *J. Phys. Chem. B* **2004**, *108* (31), 11375–11383.

(66) Forslund, R. P.; Mefford, J. T.; Hardin, W. G.; Alexander, C. T.; Johnston, K. P.; Stevenson, K. J. Nanostructured LaNiO3 Perovskite Electrocatalyst for Enhanced Urea Oxidation. *ACS Catal.* **2016**, *6* (8), 5044–5051.

(67) Zhou, W.; Sunarso, J. Enhancing Bi-Functional Electrocatalytic Activity of Perovskite by Temperature Shock: A Case Study of LaNiO3−δ. *J. Phys. Chem. Lett.* **2013**, *4* (17), 2982–2988.

(68) Lee, D. U.; Park, H. W.; Park, M. G.; Ismayilov, V.; Chen, Z. Synergistic Bifunctional Catalyst Design Based on Perovskite Oxide Nanoparticles and Intertwined Carbon Nanotubes for Rechargeable Zinc–Air Battery Applications. *ACS Appl. Mater. Interfaces* **2015**, *7* (1), 902–910.

(69) Hu, J.; Liu, Q.; Shi, Z.; Zhang, L.; Huang, H. LaNiO 3 -Nanorod/Graphene Composite as an Efficient Bi-Functional Catalyst for Zinc–air Batteries. *RSC Adv.* **2016**, *6* (89), 86386–86394.

(70) Materials   Project https://materialsproject.org/#apps/pourbaixdiagram/{"chemsys"%3A["C"]} (accessed Nov 20, 2016).

(71) Persson, K. A.; Waldwick, B.; Lazic, P.; Ceder, G. Prediction of Solid-Aqueous Equilibria: Scheme to Combine First-Principles Calculations of Solids with Experimental Aqueous States. *Phys. Rev. B* **2012**, *85* (23), 235438.

(72) Lyon, J. L.; Stevenson, K. J. Anomalous Electrochemical Dissolution and Passivation of Iron Growth Catalysts in Carbon Nanotubes. *Langmuir* **2007**, *23* (22), 11311–11318.

TOC Figure